Open Ceramics 19 (2024) 100661

Contents lists available at ScienceDirect

Open Ceramics

journal homepage: www.sciencedirect.com/journal/open-ceramics

# Spark plasma sintering of TiC with $TiAl_y$ as sintering aid: Mechanisms and microstructures

Alessandro Rizzi [a,*], María García-Fernández [b], Miguel Á. Rodríguez [b], Emanuele De Bona [a], Rodrigo Moreno [b], Mattia Biesuz [a]

[a] Department of Industrial Engineering, University of Trento, Via Sommarive 9, 38123, Trento, TN, Italy
[b] Institute of Ceramics & Glass, ICV-CSIC, Kelsen 5, 28049, Madrid, Spain

ARTICLE INFO

Handling Editor: Dr Catherine Elissalde

*Keywords:*
TiC
SPS
TiAl
Sintering
UHTCs

ABSTRACT

TiC features an interesting combination of mechanical properties, high-temperature resistance, and lightness, making it an excellent candidate for several applications in harsh environments. However, its sintering to obtain bulk components is extremely challenging. Herein, we show that titanium aluminide is a promising sintering aid for TiC (5, 10, and 20 vol% were investigated). The aluminide allows the formation of a nearly fully dense component at 1350 °C by spark plasma sintering under 80 MPa. The aluminide forms a grain boundary secondary phase that promotes the Ti diffusion: Ti from TiC can be dissolved within the $TiAl_y$ at the neck center and precipitate at the neck surface, while C can easily diffuse through the TiC lattice. Higher temperatures cause the extrusion of the aluminide out of the SPS die and its reaction with oxygen impurities. The final microstructure is constituted by nearly pure TiC with isolated alumina pockets at the triple points.

## 1. Introduction

Ultra-high temperature ceramics (UHTCs) have gained increasing interest in recent years thanks to their outstanding properties, such as very high melting temperature, combined with excellent mechanical properties, and fair thermal conductivity [1]. UHTCs are mainly carbides, nitrides, and borides of early transition metals presenting a melting temperature above 3000 °C and a service temperature in air above 2000 °C [1,2].

Among the UHTCs, titanium carbide (TiC) is of particular interest. It is a refractory Group IV interstitial carbide characterized by a cubic closed-packed structure with an FCC symmetry [3]. Its structure provides exceptional properties: very high melting temperature ($T_m = 3067$ °C [3]), fair thermal conductivity [3–5], which provides good thermal shock resistance, low density with respect to other carbides, and excellent mechanical properties [4,6], like a very high hardness (28–35 GPa [4,6]), huge elastic modulus (410–510 GPa [4,6]) and fair fracture toughness ($3.3 \pm 0.1$ MPa • $m^{0.5}$ [6]).

The combination of properties makes TiC particularly fascinating for high-temperature applications in harsh environments: such as (i) the nuclear energy field, (Gen IV Nuclear power plants) due to its compatibility with UN and UC [7–11]; (ii) the aerospace and hypersonic flight industry as thermal protection [12,13] for shielding [14,15] and aero-propulsion system [16,17]; (iii) cutting and grinding tools [18–21]; and (iv) coating and reinforcement [22–26].

The production of UHTC components is costly and exacting due to their properties: these materials are refractory, chemically inert, exhibiting strong covalent bonds, and possessing a general tendency to decompose upon melting. Consequently, common metallurgical processes, such as casting or forging, are not suitable and also powder consolidation by sintering is very challenging. These factors have limited for long the development and commercial applications of these materials [3].

Several methods exist for the synthesis of titanium carbide powder [4]: including the carbothermal reduction [27–29], pyrolysis of oxygen-containing metal-organic polymeric precursors [29], gas phase reaction of $TiCl_4$ and hydrocarbons [30], Mg-thermal reduction of vaporized $TiCl_4 + CCl_4$ solution [31], sol-gel process [27,32,33], mechanical alloying [34–36] and Self-propagating High-temperature Synthesis (SHS) [37–41]. Among them, SHS is of particular interest. It is an efficient and energy-saving method allowing the production in a few seconds of high melting point compounds which form through an exothermic reaction involving the forming elements.

The most commonly employed consolidation technique for TiC is

---

* Corresponding author.
*E-mail address:* Alessandro.rizzi999@gmail.com (A. Rizzi).

https://doi.org/10.1016/j.oceram.2024.100661
Received 13 June 2024; Received in revised form 2 August 2024; Accepted 19 August 2024

Spark Plasma Sintering (SPS) [7,42]. In SPS densification is aided by the application of an external pressure and the system is subjected to a low-voltage direct pulsed current [43–45]. The application of a uniaxial mechanical load (typically between 50 and 250 kN) improves the densification kinetics enhancing the driving force for sintering [44]. Furthermore, in electrically-conductive samples, additional densification-enhancing mechanisms might be activated including electromigration [46–48]. Directional electromigration-enhanced interdiffusion in the Cu–Ni system [49]. The sintering process can be performed under vacuum or protective gas at atmospheric pressure [50]. Due to the direct Joule heating of the graphite tooling where the ceramic powder is introduced, SPS allows heating rates potentially as high as 1000 °C/min for small samples, which makes it possible to significantly reduce the sintering time and consequently the energy costs [51]. Despite the external pressure application, temperatures exceeding 1800 °C are usually needed to densify TiC even in SPS [7,52,53].

In this work, we explore the use of titanium aluminide (TiAl) as a sintering aid for TiC in SPS. The choice is based on the fact that TiAl is lightweight and largely employed in aerospace and automotive high-temperature applications [54–56], where it can be coupled with TiC due to its similar thermal expansion coefficient and chemical compatibility [57–59].

Furthermore, TiAl melts at 1460 °C [60] hence one could expect the activation of liquid phase sintering mechanisms. Herein, we aimed to identify the physical/chemical mechanisms activated by the aluminide phase's presence on the Ti carbide's sintering.

## 2. Materials and methods

### 2.1. Synthesis

TiC powder doped with 5 vol%, 10 vol% and 20 vol% of TiAl was produced using the following raw materials: Ti powder (84 µm, specific surface area SSA = 0.03 $m^2/g$, purity >98 %, William Rowland Ltd., UK), graphite powder (1.7 µm, SSA = 27 $m^2/g$ purity> 99.6 %, Sofacel, Spain) and aluminum (16 µm, Alcoa, USA).

The elemental powders were weighted in stoichiometric proportion and mixed for 1 h in a powder blender mixer Turbula® (Switzerland) to obtain batches of 200 g.

Then, the self-propagating high-temperature synthesis (SHS) was performed in a graphite container inside a closed methacrylate box using tungsten filaments under Ar atmosphere. The applied voltage to the W filament, used for ignition, was 20 V and the reaction time least a few seconds.

The SHS method allowed the synthesis of a large amount of powder in a very short time and an efficient conversion rate due to the elevated temperatures reached because of the high exothermicity of these reactions and the accumulation of heat.

TiC powder was obtained by reaction of Ti and graphite while the composite TiC–TiAl was obtained by adding Al powder in such a concentration as to obtain 5 vol%, 10 vol% and 20 vol% of TiAl according to the stoichiometric reaction. It is important to mention that the adiabatic temperature of combustion for TiC and for TiAl is 3209 K [61] and 1518 K [62], respectively.

The powder obtained by SHS was then attrition milled in isopropanol using a nylon-coated jar and rotor arms and Y-TZP balls with 5 mm in diameter as milling medium. After that, the powder was dried in an oven overnight and eventually sieved with a 63 µm nylon mesh.

The evolution of the TiC–TiAl particle size during the milling process was monitored and analyzed by laser diffraction (Mastersizer S, Malvern, U.K.), using aqueous suspensions diluted to 0.1 g/L at a fixed interval time ranging from 0 to 420 min, depending on the powder composition and doping level.

### 2.2. Spark plasma sintering

TiC–TiAl powders were used to obtain a cylinder with a diameter of 20 mm and a height of 6 mm. The samples were sintered by spark plasma sintering (SPS) using a Dr. Sinter SPS-1050-CE (Japan) furnace, in which the powders were loaded in 20 mm graphite dies, lined with graphite foils, and covered by graphite blankets. The temperature was monitored through an optical pyrometer, which works in the infrared, starting from 570 °C.

The sintering experiments were carried out using 100 °C/min as the heating rate, a dwell at high temperature of 5 min and applying an external pressure of 80 MPa. The sintering temperatures were modified for each composition to achieve the highest possible densification (Table 1).

### 2.3. Samples characterization

Archimedes' method, as reported in ASTM C830, was exploited to measure the bulk density, the relative density, and the open porosity of the samples. Water was used as the buoyancy medium and a balance with a sensitivity of 0.1 mg was employed.

The microstructure of polished samples was observed by Scanning Electron Microscopy (SEM) using a JEOL JSM-5500 (Japan) equipment. EDXS micro-analysis was performed to evaluate the elemental distribution, EDXS was carried out in a JEOL JSM-IT300 LW SEM (Japan) equipped with a Bruker XFlash 630 M detector (Germany) operating at 20 keV.

The X-ray diffraction (XRD) was performed both on the powder (after the milling process) before sintering and on the sintered samples using a Bruker D8 Advance (Germany) diffractometer equipped with Cu Kα X-ray source. The measurements were performed in the $2\theta = 10^\circ$–$80^\circ$ range, step size = 0.05° with a 1.5 s/step dwell. The quantitative phase analysis and the lattice parameters were evaluated by exploiting the Rietveld refinement using the MAUD® software [63].

The mechanical properties exhibited by TiAl-doped TiC specimens were also evaluated by measuring the Vickers hardness, using a Tecmet Future-Tech FM-310 microhardness tester (Italy) with a load of 0.2 kg. The values presented in this work are the averages of 10 measurements per sample. The samples were preliminarily polished using SiC grinding papers (up to grit 1200) and then diamond solution on specific grinding papers down to 1 µm.

In the following parts of this paper, we will refer to the TiAl-doped TiC samples as TiCxxTiAl, where xx indicates the theoretical volume fraction of TiAl in the mixture.

## 3. Results

After the SHS, the powder is constituted by a mixture of TiC, TiAl, TiO and unreacted carbon (Fig. 1). A shoulder in the high-angle region of the main TiC phase suggests the presence of some substoichiometric TiC

**Table 1**
SPS sintering conditions for TiC doped with 5 vol%, 10 vol% and 20 vol% of TiAl.

| | Temperature [°C] | Pressure [MPa] | Holding time [min] | Heating rate [°C/min] |
|---|---|---|---|---|
| ***TiC+5 vol% TiAl*** | *1800* | *80* | *5* | *100* |
| ***TiC+10 vol %TiAl*** | *1650* | *80* | *5* | *100* |
| | *1700* | *80* | *5* | *100* |
| | *1800* | *80* | *5* | *100* |
| | *1150* | *80* | *5* | *100* |
| | *1350* | *80* | *5* | *100* |
| ***TiC+20 vol %TiAl*** | *1500* | *80* | *5* | *100* |
| | *1550* | *80* | *5* | *100* |
| | *1700* | *80* | *5* | *100* |

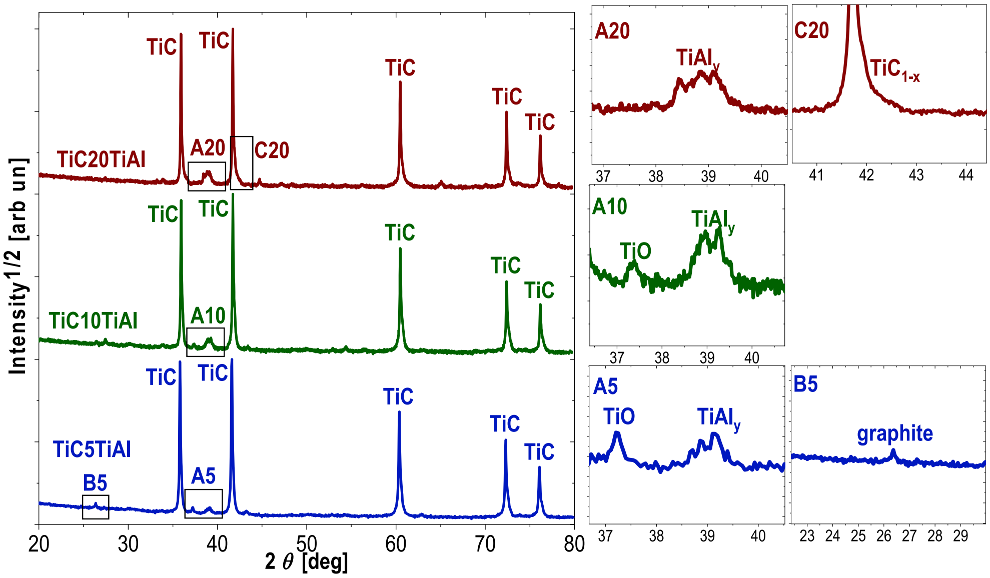

**Fig. 1.** XRD analysis pattern of TiC doped with 5 vol%, 10 vol% and 20 vol%, where the particular of Al-rich TiAl peak splitting (A5, A10 and A20), the unreacted carbon (B5) and non-stoichiometric $TiC_{1-x}$ (C20) are also highlighted.

(i.e., $TiC_{1-x}$). Based on the Rietveld refined cell parameter data we can estimate the non-stoichiometric phase to be characterized by a C/Ti molar ratio of about 0.59 ± 0.2 for all the tested compositions [64]. The presence of the aluminide phase can be clearly detected in the diffraction patterns (see for instance the peaks at 39°) and obviously increases with the Al-doping level in the system. The exact stoichiometry of the aluminide cannot be determined as TiAl, $TiAl_2$, and $TiAl_3$ have similar diffraction patterns, for such reason we will label the aluminide and $TiAl_y$ in the following. As minor phases, we detected some unreacted carbon (only in the sample with 5 vol% of doping) and some rocksalt TiO.

The particle size after SHS is unsuitable for sintering as they are in the order of several tens of micrometers (see the SEM micrographs in Fig. 2). Fig. 3 reports particle size evolution during milling in isopropanol. The particle size substantially decreases with the milling time for all the compositions. However, it scales with the TiAl doping level (the higher the doping level the larger the particles after milling). In all the cases, the final particle size is < 5 μm, and at least 4 h were needed to mill the powder before SPS.

The sintering curves obtained from the displacement of the SPS piston corrected for the thermal expansion are reported in Fig. 4. We can observe that the $TiAl_y$ addition facilitates the consolidation by decreasing the onset temperature for sintering (down to ≈900 °C) and increasing the displacement (densification) rate. The final shrinkage increases with the aluminide content. The shape of the sintering curves appears "non-regular", i.e., it does not follow the usual sigmoidal plot with a single inflection point but several changes in slope and concavity can be spotted. To understand the evolution of the material during the sintering process, we decided to SPS at different temperatures. Specifically, most of the analysis focuses on the Ti20TiAl composition as the influence of the sintering aid is much more relevant, making the different steps of the firing process and the related effects more evident and easy to observe.

Fig. 5 reports the relative bulk density evolution for samples sintered at different temperatures. We can observe a monotonical increase in the sample density with the sintering temperature. It is quite surprising to observe that the sample containing 20 vol% of TiAl already achieved relatively good densification at only 1150 °C (≈85 % relative density) and most of the sintering is accomplished at 1350 °C(≈97 % relative density). Such temperature is well below the melting point of the aluminide phase. There is no substantial density evolution between 1350 and 1550 °C for the TiC20TiAl composition, and eventually, a small increase in density is observed between 1550 and 1700 °C. Remarkably, the pure TiC sample sintered at 1900 °C exhibits a relative density lower than TiC20TiAl at 1700 °C.

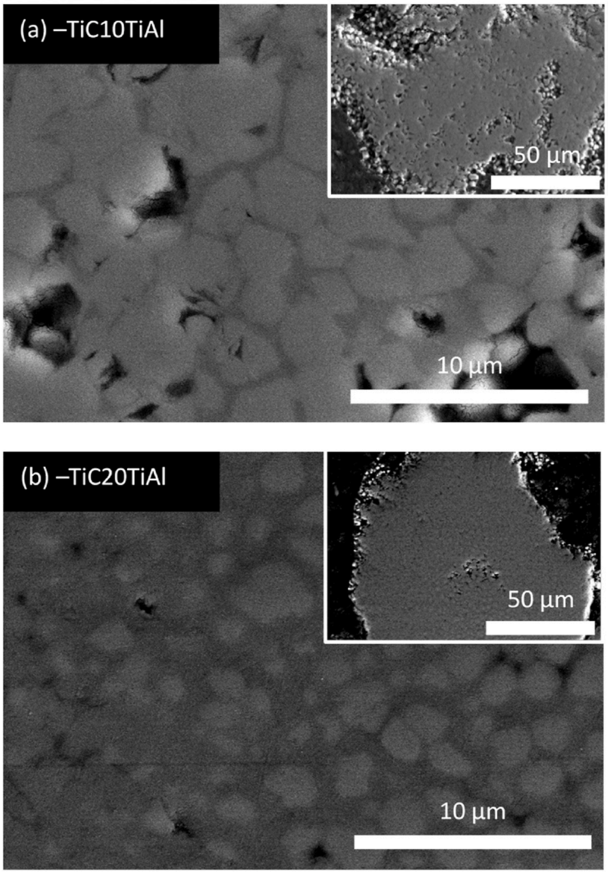

**Fig. 2.** SEM images of (a) TiC10TiAl and (b) TiC20TiAl polished powder after SHS before milling.

Fig. 6 reports the Al content detected by EDXS on the sintered

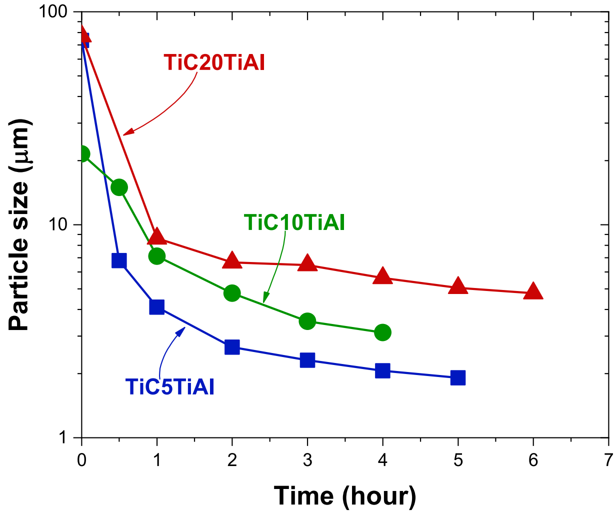

**Fig. 3.** Particle size evolution during milling of TiAl-doped TiC powders.

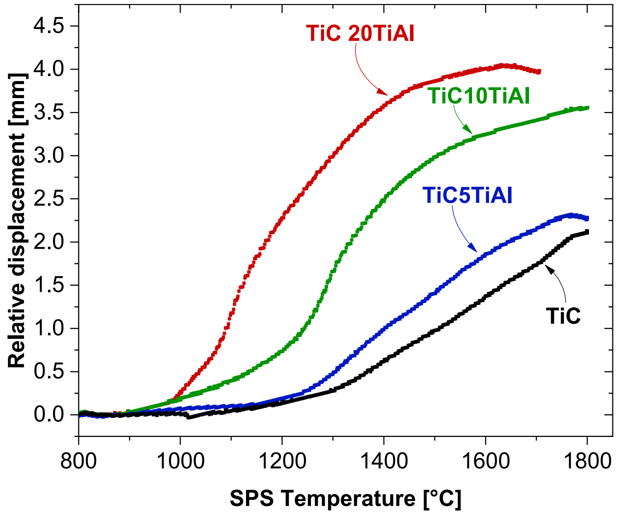

**Fig. 4.** SPS sintering curves (relative displacement vs. temperature) of TiAl-doped TiC samples.

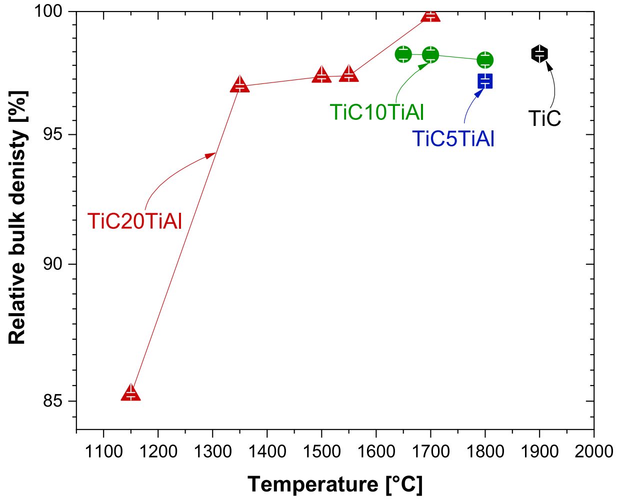

**Fig. 5.** Relative bulk density evolution with respect to the sintering temperature measured by Archimedes' method.

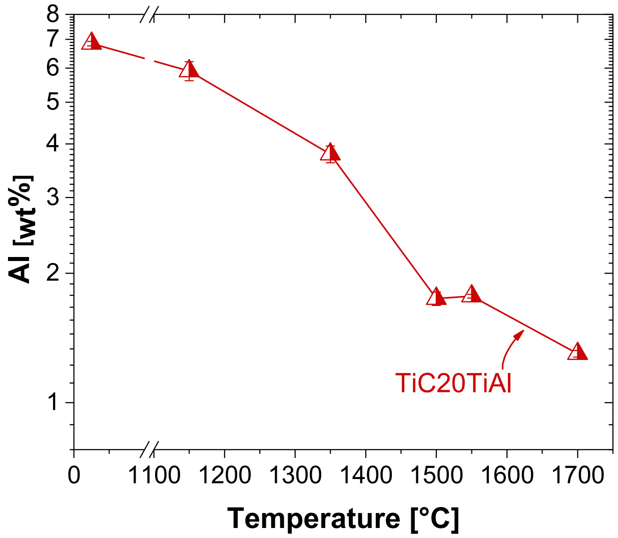

**Fig. 6.** Al content evolution during sintering measured by EDXS analysis in TiC20TiAl.

TiC20TiAl samples as a function of the SPS temperature. We can observe that the Al content decreases increasing the firing temperature, thus pointing out an evolution in the material composition. After firing at 1700 °C, the Al content is about 1/5 of the starting one. Such evolution in the composition was accounted for in the calculation of the theoretical density used to estimate the relative density in Fig. 5.

The microstructural evolution at different sintering temperatures for TiC20TiAl is reported in Fig. 7. The micrographs refer to polished samples and are substantially consistent with the density data reported in Fig. 5. The microstructures are clearly biphasic, featuring a darker Al-rich phase and a brighter compound which is the TiC. Already at 1150 °C, the material is substantially consolidated with indeed some residual porosity. Despite some sintering happening at 1150 °C (density ≈85 %), the shape of the TiC particles is still irregular and characterized by sharp edges. At 1350 °C, the aluminum-rich phase is located at the grain boundaries between the TiC particles and at the triple points. The microstructure is nearly fully dense. At 1550 °C, the amount of dark (al-rich) phase is substantially reduced, but a thin layer of it can still be observed at the grain boundary and triple points. Finally, at 1700 °C the aluminum-rich phase collapses in spherical clusters.

To confirm the correct identification of the two phases in Fig. 7, we performed EDXS analysis on the samples treated at 1150 and 1350 °C. At 1150 °C, the Al-rich phase segregates largely in the porosity between the TiC grains. The comparison between the Al and Ti content in area 1 (inside a grain) and area 2 (pore) as well as the EDXS elemental maps, confirms the partial extrusion of Al toward the pores (Fig. 8(a) and (b)). On the other hand, the EDXS line scan confirms that the continuous grain boundary phase at 1350 °C is actually Al-rich (Fig. 9(a) and (b)). Finally, at 1550 °C aluminum is localized in rounded clusters (Fig. 10), where locally the Ti counts drop nearly to zero (i.e., the Al-rich region does not contain Ti in the EDXS map).

A comparison of the XRD pattern of the different samples is reported in Fig. 11. The Rietveld refinement results are summarized in Table 2. We can observe that (i) the signal of the sub-stoichiometric TiC rapidly quenchs during the thermal treatments; (ii) the aluminide gets partially oxidized already at 1500 °C forming α-$Al_2O_3$; (iii) the metastable TiO phase disappears.

A comparison between the Vickers hardness of the TiC specimens doped with different amounts of TiAl (5 vol%, 10 vol% and 20 vol%) is reported in Fig. 12, in which the Vickers hardness, measured with a load of 0.2 kg, is highlighted as a function of the relative density. In general, the hardness of the samples decreases increasing the amount of sintering aids.

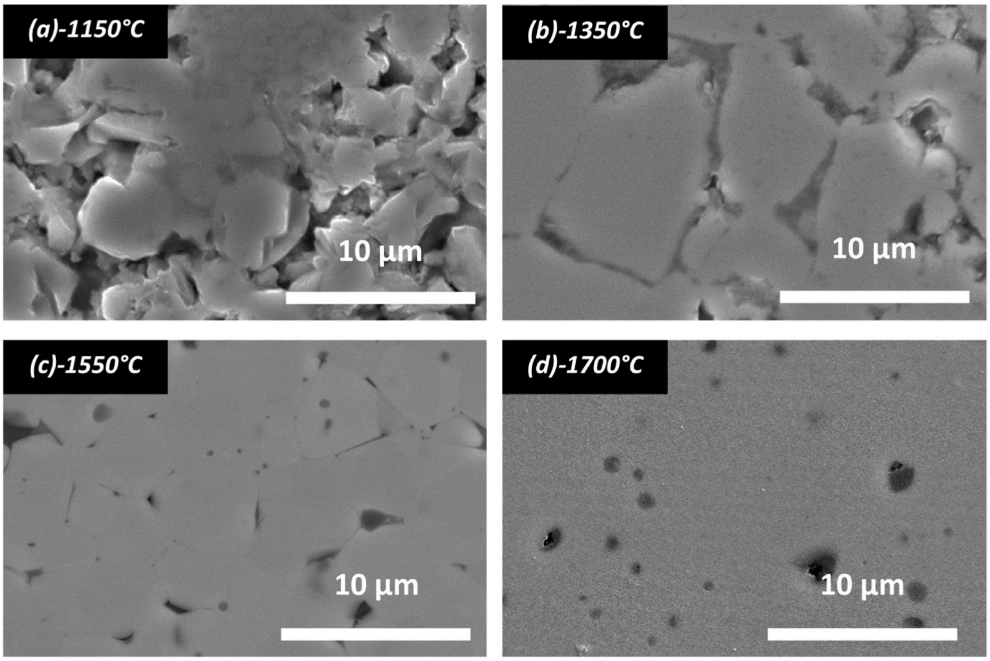

**Fig. 7.** SEM images of TiC doped with 20 vol% of TiAl at (a) 1150 °C, at (b) 1350 °C, at (c) 1550 °C and at (d) 1700 °C.

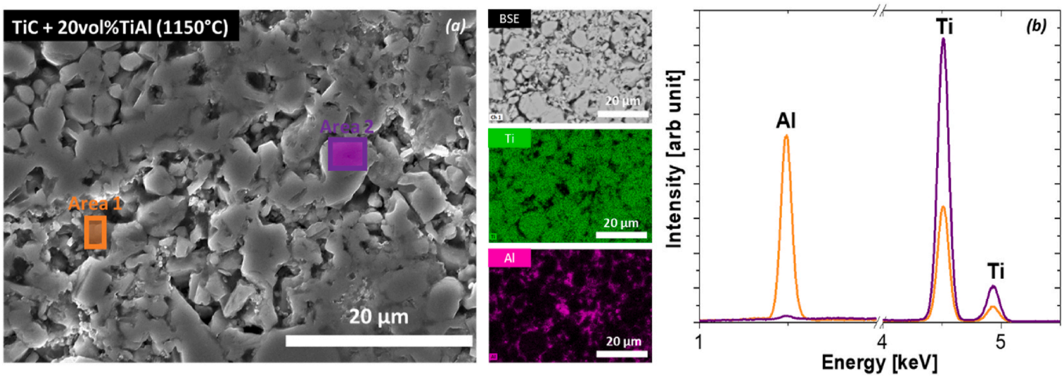

**Fig. 8.** (a) SEM image and EDXS map analysis of TiC + 20 vol% TiAl sintered at 1150 °C by SPS and (b) comparison between the Al and Ti content of area 1 (orange) and area 2 (purple) highlighting, respectively, the space between grains and TiC grains, obtained by EDXS analysis. (For interpretation of the references to colour in this figure legend, the reader is referred to the Web version of this article.)

## 4. Discussion

SHS allowed the synthesis of TiC-TiAl$_y$ powders with minor contaminants. The main impurities are unreacted graphite and TiO. TiO forms by the reaction between titanium and oxygen impurities in the SHS chamber or even as a result of O contamination in the starting powder (like the surface oxide layer expected in Ti and Al powder). The presence of unreacted graphite was observed only in the case of the TiC5TiAl powder, i.e., in the powder with the lowest TiAl content. The presence of the molten aluminide, during the SHS synthesis, facilitates the reaction between TiC and C providing a fast diffusion path, hence the reaction was fully completed without residual graphite for TiAl doping $\geq$10 vol%. The formation of a liquid aluminide phase in SHS can be inferred from the microstructures in Fig. 2, where the TiC grains appear rounded and grown inside an Al-rich isotropic matrix.

The presence of unreacted graphite contributes to the formation of sub-stoichiometric TiC, which is actually more abundant in the TiC5TiAl composition where unreacted C was detected. Furthermore, the possible formation of secondary aluminide phases, like TiAl$_2$ and TiAl$_3$, leaves some extra Ti available for the TiC formation (the initial mixture was prepared assuming that only TiAl forms) causing a disproportion between Ti and C in the carbide. The formation of TiC$_{1-x}$ is however not particularly surprising as all the rock salt interstitial carbides of group 4 (TiC, ZrC, HfC) are largely non-stoichiometric and can accommodate easily carbon vacancies [1,3].

The sintering curves (Fig. 4) reveal two interesting features. The first is that the aluminide impacts on sintering well before its melting point, and the second is that the sintering shrinkage increases increasing the TiAl$_y$ content. To exclude the formation of different liquids originating from low-temperature reactions in the Ti–C–Al phase diagram [60] a TGA/DTA was carried out under 50 °C/min up to 1350 °C (Fig. S1 in Supplementary Material). No endothermic peaks were detected in this temperature region, where the material densified. This seems to exclude the activation of substantial amounts of liquid phase sintering during SPS.

As the final density approaches the theoretical one in all the samples in Fig. 5, one would expect similar final sintering displacement (the amount of tested material was always similar and there are no specific reasons to assume substantial differences in the green density). The fact that increasing the TiAl$_y$ content the sintering displacement is higher

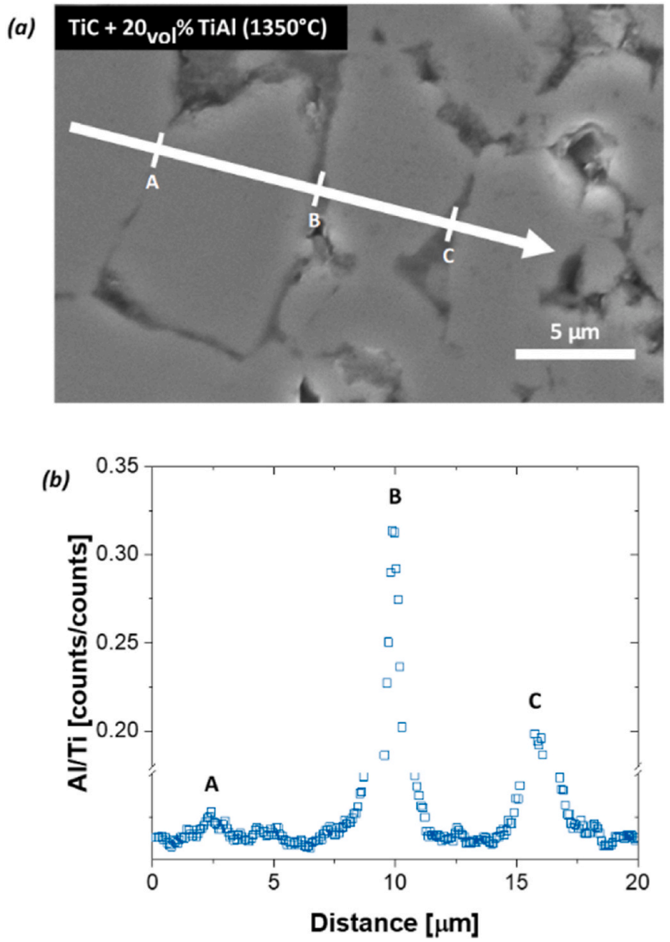

**Fig. 9.** (a) SEM image of TiC + 20 vol% TiAl sintered at 1350 °C and (b) line scan Al/Ti ratio obtained by EDXS analysis of TiC + 20 vol% TiAl sintered at 1350 °C.

implies that some material is extruded out of the SPS die and this agrees with the EDXS data in Fig. 6 which proves that part of the aluminum is lost while sintering. Therefore, a higher Al load in the starting powder results in larger shrinkage as more material is lost in SPS.

Such a result is of some interest because $TiAl_y$ can act as a very effective sintering additive, but in the final microstructures, the aluminide nearly completely disappears as it is extruded out of the die and also partially converted to alumina (see the XRD in Fig. 11) which is indeed more refractory than $TiAl_y$ ($T_{m,TiAl} = 1460$ °C [60], $T_{m,Al2O3} = 2051$ °C [65]). The alumina formation can be explained based on the high affinity between Al and O contamination in the SPS atmosphere. Moreover, Alumina [53,60] segregates in closed and isolated pockets at the end of the sintering process due to the Rayleigh instability of the percolative film. The reduced sintering aid content, its conversion to alumina, and its non-percolative distribution in the sample are valuable results: the presence of a continuous TiAl grain boundary phase would limit the operative temperature of the components and reduce its refractory properties. In the next future, further works could be focused on the investigation of the high-temperature properties of the sintered materials.

The other key result is that the material is already nearly fully dense well before the melting point of the $TiAl_y$, with a sintering onset around 900 °C. For instance, a density of already ≈85 % is achieved at 1150 °C for the TiC20TiAl composition. At such temperatures, we expect that TiC marginally contributes to the densification. This statement is supported by the fact that the pure TiC sintering curve (Fig. 4) does not show any substantial effect below 1200 °C. Furthermore, the micrograph of the TiC20TiAl sample sintered at 1150 °C (≈85 % dense) features irregular particles with sharp edges originated from the milling process. Indeed, such features are the first ones typically evolving when self-diffusion is activated. Their presence in the sintered component suggests that TiC only marginally participates in the densification process. On the other hand, at these temperatures, $TiAl_y$ could deform under the effect of the external pressure application [66]. Hence, the $TiAl_y$ can be partially extruded from the region between the "rigid" TiC particles to the surface of the pores. The phenomenon is confirmed by the EDXS maps in Fig. 8 as an abundant presence of Al was detected in the pores.

At higher temperatures also TiC starts to participate in sintering. This is suggested by the high densification level obtained at 1350 °C (≈97 %)

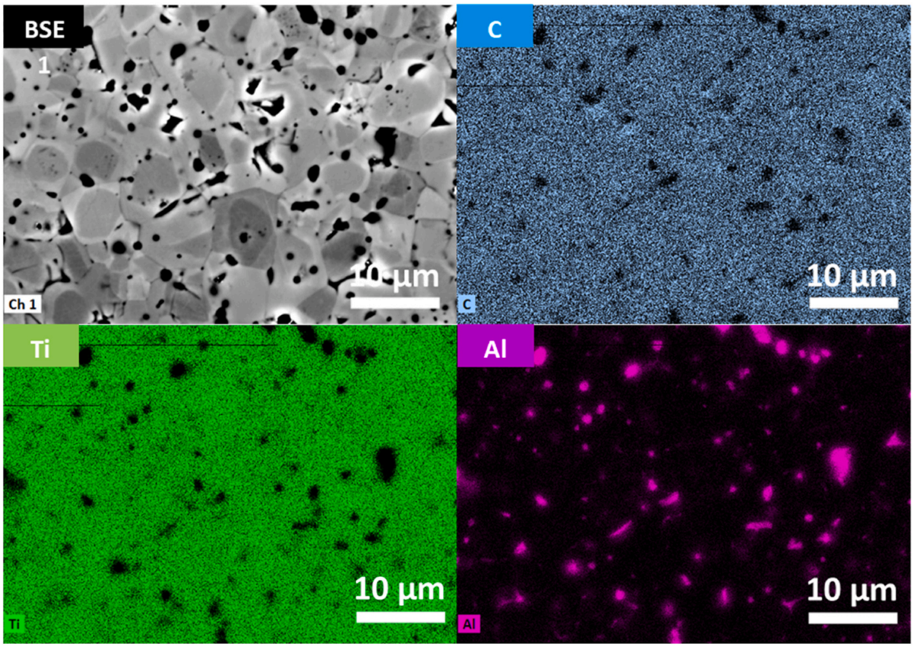

**Fig. 10.** EDXS map analysis of TiC +20 vol% TiAl sintered at 1550 °C.

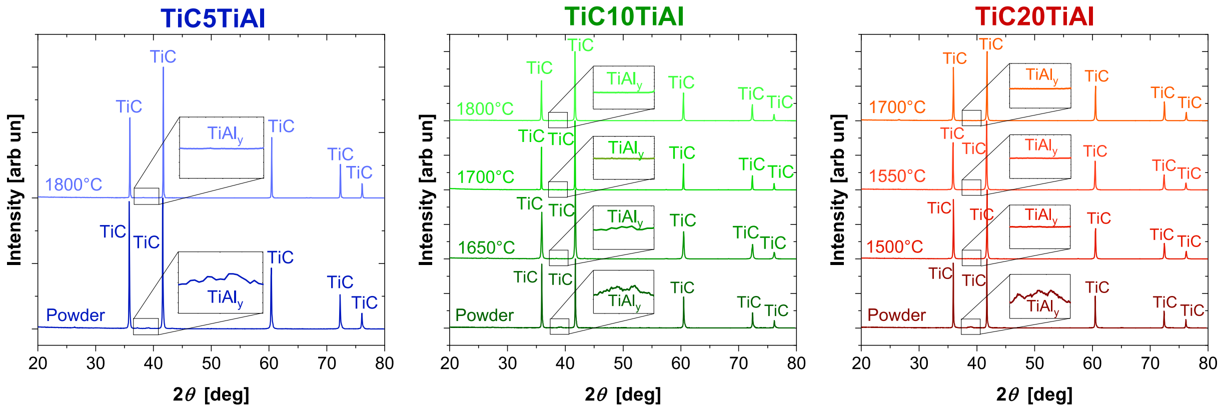

**Fig. 11.** XRD pattern comparison of TiC doped with 5 vol% (blue), 10 vol% (green) and 20 vol% (red) of TiAl. (For interpretation of the references to colour in this figure legend, the reader is referred to the Web version of this article.)

**Table 2**
Rietveld refinement quantitative analysis of TiAl-doped samples subjected to XRD analysis. Note that content below 3 wt% of the data is only indicative and subjected to large errors.

| Composition | Temperature [°C] | TiC [wt%] | $TiC_{1-x}$ [wt%] | $TiAl_y$ [wt%] | TiO [wt%] | $Al_2O_3$ [wt%] | Graphite [wt%] |
|---|---|---|---|---|---|---|---|
| ***TiC+5 vol%TiAl*** | ***25*** | 73.7 | 23.3 | 0.5 | 0.6 | 0 | 1.9 |
| | ***1800*** | 92 | 4 | 0.8 | 0 | 1.6 | 1.6 |
| ***TiC+10 vol%TiAl*** | ***25*** | 81.2 | 15.5 | 2.7 | 0.6 | 0 | * |
| | ***1650*** | 94 | 3.4 | 0.6 | 0 | 2 | * |
| | ***1700*** | 94.9 | 1.7 | 0.6 | 0 | 2.8 | * |
| | ***1800*** | 94.1 | 2.5 | 0.7 | 0 | 2.7 | * |
| ***TiC+20 vol%TiAl*** | ***25*** | 79.1 | 14.7 | 4.4 | 1.8 | 0 | * |
| | ***1500*** | 90.4 | 6.7 | 0.7 | 0 | 2.2 | * |
| | ***1550*** | 90.3 | 6.4 | 0.8 | 0 | 2.5 | * |
| | ***1700*** | 93.3 | 3.2 | 0.5 | 0 | 3 | * |

(*) Refers to a weight percentage well below 1 wt%.

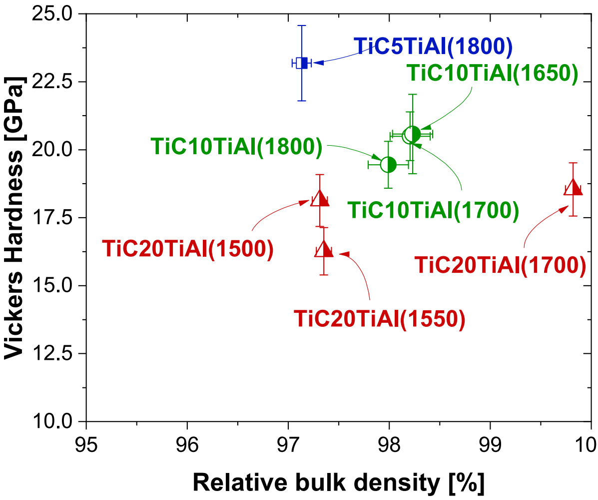

**Fig. 12.** Vickers hardness (0.2 kg) of TiC5TiAl (blue), TiC10TiAl (green) and TiC20TiAl (red) sintered by SPS at different temperatures, as a function of the relative bulk density. (For interpretation of the references to colour in this figure legend, the reader is referred to the Web version of this article.)

and by the substantial changes in the particle's shape. In this temperature interval, the aluminide acts as an effective sintering aid, operating in the solid state (TiAl melts only at 1460 °C and no sign of melting can be detected in Fig. S1 in Supplementary Material). The $TiAl_y$ effect seems not related to bulk interaction with TiC, for instance, changing the point defect chemistry by forming a solid solution. This can be inferred by the absence of any TiC XRD peak position shift during sintering and by the fact that the solubility of Al in TiC is limited [60]; moreover, no clear EDXS Al signal from the bulk of TiC grains was detected. On the other hand, the Al-rich phase forms a continuous path (Fig. 7(b)) on the grain boundaries and triple points which could promote sintering.

The sintering of TiC is dominated by the diffusion of cations, while the diffusivity of carbon is several orders of magnitude faster [67]. A comparison between the self-diffusion coefficient of Ti and C in TiC [67] and of Ti and Al in TiAl [68] is reported in Fig. 13.

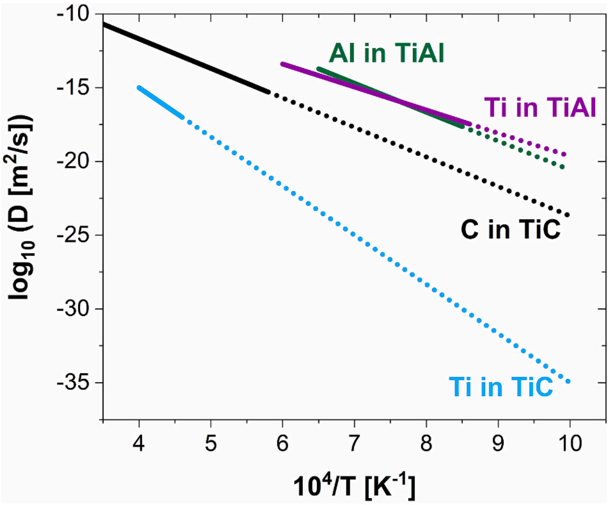

**Fig. 13.** Self-diffusion coefficient of Ti in TiAl and TiC and C in TiC. (Data taken from the literature [67,68], continuous line for experimental data and dotted line for extrapolated data).

The presence of the continuous aluminide phase at the grain boundary could allow the dissolution of Ti from the TiC crystal at the neck center, its fast diffusion through the aluminide [68], and its precipitation at the neck surface. This is facilitated by the fact that Ti can easily dissolve inside the Ti-aluminide where lattice sites matching the Ti radius and charge are available. The suggested mechanism is substantially analogous to what was observed in liquid phase sintering, with the major difference that the fast diffusion avenue is not in the liquid but in the solid state (i.e., at 1350 °C we are still below the melting point of the aluminide). The other difference is that we do not expect carbon to diffuse through the same path as its solubility in $TiAl_y$ is modest (usually $< 1$ at% [69]) and, more importantly, it already has a fast diffusion path through the TiC lattice (Fig. 13).

When considering the TiC20TiAl composition the densification is substantially completed at 1350 °C, however, the sintering curve still shows a substantial displacement at higher temperatures. This is related only to the extrusion of the Al-rich phase out of the die as already discussed. In fact, up to 1550 °C there is no further density improvement (Fig. 5). In this temperature region, the Al content dramatically drops and the Al-containing phase progressively clusters in spherical regions leading to the final microstructure constituted by insulated corundum regions within a TiC matrix.

The Vickers hardness (Fig. 12) decreases when increasing the initial doping content, in accordance with the ones reported in the literature [1,4,6]. This can be attributed to the fact that the dopant possesses a hardness lower than the TiC.

## 5. Conclusions

Titanium aluminide serves as an effective sintering aid for TiC in SPS. The aluminides form a continuous grain boundary phase between TiC particles facilitating sintering mainly in the solid state. It is argued that Ti from TiC can be dissolved in $TiAl_y$ at the neck center and precipitate at the neck surface, while C can easily diffuse through the TiC lattice. The combination of fast diffusion of Ti in the solid aluminide grain boundary phase and C through the TiC lattice provide enhanced densification at temperatures <1350 °C (SPS under 80 MPa).

At higher temperatures, most of the Al is lost and extruded out of the SPS die. The final microstructure after sintering at temperatures exceeding 1500 °C is mainly constituted by corundum pockets (formed by the reaction of aluminum with O impurities) within a TiC matrix. The aluminide addition therefore allows a substantial improvement of the sintering behaviour but its evolution does not leave a weak and non-refractory percolative grain boundary phase after sintering.

## CRediT authorship contribution statement

**Alessandro Rizzi:** Writing – original draft, Project administration, Formal analysis, Data curation, Conceptualization. **María García-Fernández:** Supervision, Methodology, Data curation. **Miguel Á. Rodríguez:** Resources. **Emanuele De Bona:** Supervision, Investigation, Formal analysis, Data curation. **Rodrigo Moreno:** Writing – review & editing, Validation, Supervision, Project administration. **Mattia Biesuz:** Writing – review & editing, Validation, Supervision, Project administration, Funding acquisition, Formal analysis, Conceptualization.

## Declaration of competing interest

The authors declare the following financial interests/personal relationships which may be considered as potential competing interests: Alessandro Rizzi reports administrative support, article publishing charges, equipment, drugs, or supplies, and travel were provided by JECS Trust. If there are other authors, they declare that they have no known competing financial interests or personal relationships that could have appeared to influence the work reported in this paper.

## Acknowledgments

The authors are grateful to the JECS Trust for funding the visit of Alessandro Rizzi to the ICV in Madrid, from July until September 2023 (Contract No. 2023340) and to Grant PID2021-124521OB-100 funded by MCIN/AEI/10.13039/501100011033 and "ERDF A way of making Europe".

## Appendix A. Supplementary data

Supplementary data to this article can be found online at https://doi.org/10.1016/j.oceram.2024.100661.

## References

[1] W.G. Fahrenholtz, E.J. Wuchina, W.E. Lee, Y. Zhou, Ultra-High Temperature Ceramics, Wiley, 2014, https://doi.org/10.1002/9781118700853.
[2] J. Binner, M. Porter, B. Baker, J. Zou, V. Venkatachalam, V.R. Diaz, A. D'Angio, P. Ramanujam, T. Zhang, T.S.R.C. Murthy, Selection, processing, properties and applications of ultra-high temperature ceramic matrix composites, UHTCMCs – a review, Int. Mater. Rev. 65 (2020) 389–444, https://doi.org/10.1080/09506608.2019.1652006.
[3] H.O. Pierson, Handbook of Refractory Carbides and Nitrides: Properties, Characteristics, Processing and Applications, William Andrew, 1996.
[4] M. Mhadhbi, Titanium carbide: synthesis, properties and applications, Brilliant Engineering 2 (2020) 1–11, https://doi.org/10.36937/ben.2021.002.001.
[5] K.-T. Chiang, Modeling and analysis of the effects of machining parameters on the performance characteristics in the EDM process of $Al_2O_3$+TiC mixed ceramic, Int. J. Adv. Des. Manuf. Technol. 37 (2008) 523–533, https://doi.org/10.1007/s00170-007-1002-3.
[6] S.P. Buyakova, E.S. Dedova, D. Wang, Y.A. Mirovoy, A.G. Burlachenko, A. S. Buyakov, Phase evolution during entropic stabilization of ZrC, NbC, HfC, and TiC, Ceram. Int. 48 (2022) 11747–11755, https://doi.org/10.1016/j.ceramint.2022.01.033.
[7] L. Cheng, Z. Xie, G. Liu, W. Liu, W. Xue, Densification and mechanical properties of TiC by SPS-effects of holding time, sintering temperature and pressure condition, J. Eur. Ceram. Soc. 32 (2012) 3399–3406, https://doi.org/10.1016/j.jeurceramsoc.2012.04.017.
[8] P. Hejzlar, M.J. Pope, W.C. Williams, M.J. Driscoll, Gas cooled fast reactor for generation IV service, Prog. Nucl. Energy 47 (2005) 271–282, https://doi.org/10.1016/j.pnucene.2005.05.077.
[9] J.H. Sinclair, L.R. Center, Compatibility of Refractory Materials for Nuclear Reactor Poison Control Systems, National Aeronautics and Space Administration, 1974. https://books.google.it/books?id=kLTqRSnUphQC.
[10] M.K. Meyer, R. Fielding, J. Gan, Fuel development for gas-cooled fast reactors, J. Nucl. Mater. 371 (2007) 281–287, https://doi.org/10.1016/j.jnucmat.2007.05.013.
[11] R. Fielding, M. Meyer, J.-F. Jue, J. Gan, Gas-cooled fast reactor fuel fabrication, J. Nucl. Mater. 371 (2007) 243–249, https://doi.org/10.1016/j.jnucmat.2007.05.011.
[12] A. Nisar, R. Hassan, A. Agarwal, K. Balani, Ultra-high temperature ceramics: aspiration to overcome challenges in thermal protection systems, Ceram. Int. 48 (2022) 8852–8881, https://doi.org/10.1016/j.ceramint.2021.12.199.
[13] R. Savino, L. Criscuolo, G.D. Di Martino, S. Mungiguerra, Aero-thermo-chemical characterization of ultra-high-temperature ceramics for aerospace applications, J. Eur. Ceram. Soc. 38 (2018) 2937–2953, https://doi.org/10.1016/j.jeurceramsoc.2017.12.043.
[14] O. Uyanna, H. Najafi, Thermal protection systems for space vehicles: a review on technology development, current challenges and future prospects, Acta Astronaut. 176 (2020) 341–356, https://doi.org/10.1016/j.actaastro.2020.06.047.
[15] S.M. Johnson, M. Gasch, J.W. Lawson, M.I. Gusman, M.M. Stackpoole, Recent Developments in Ultra High Temperature Ceramics at NASA Ames, 2009.
[16] P. Thakre, V. Yang, Chemical erosion of carbon-carbon/graphite nozzles in solid-propellant rocket motors, J. Propul. Power 24 (2008) 822–833, https://doi.org/10.2514/1.34946.
[17] S.R. Levine, E.J. Opila, M.C. Halbig, J.D. Kiser, M. Singh, J.A. Salem, Evaluation of ultra-high temperature ceramics foraeropropulsion use, J. Eur. Ceram. Soc. 22 (2002) 2757–2767, https://doi.org/10.1016/S0955-2219(02)00140-1.
[18] F. Gong, X. Ni, G. Liu, C. Liu, J. Sun, Cutting performance and failure mechanisms of $TiB_2$-TiC-$Al_2O_3$ multi-dimensional gradient ceramic tool in intermittent turning of hardened steel, Int. J. Refract. Metals Hard Mater. 118 (2024) 106438, https://doi.org/10.1016/j.ijrmhm.2023.106438.
[19] M. Cheng, H. Liu, B. Zhao, C. Huang, P. Yao, B. Wang, Mechanical properties of two types of $Al_2O_3$/TiC ceramic cutting tool material at room and elevated temperatures, Ceram. Int. 43 (2017) 13869–13874, https://doi.org/10.1016/j.ceramint.2017.07.110.
[20] B. Liu, W. Wei, Y. Gan, C. Duan, H. Cui, Preparation, mechanical properties and microstructure of $TiB_2$ based ceramic cutting tool material toughened by TiC whisker, Int. J. Refract. Metals Hard Mater. 93 (2020) 105372, https://doi.org/10.1016/j.ijrmhm.2020.105372.
[21] X. Wang, J. Zhao, Y. Gan, X. Tang, S. Gai, X. Sun, Cutting performance and wear mechanisms of the graphene-reinforced $Al_2O_3$-WC-TiC composite ceramic tool in

turning hardened 40Cr steel, Ceram. Int. 48 (2022) 13695–13705, https://doi.org/10.1016/j.ceramint.2022.01.251.

[22] H. Wu, L. Wang, S. Zhang, C.L. Wu, C.H. Zhang, X.Y. Sun, Corrosion and cavitation erosion behaviors of laser clad FeNiCoCr high-entropy alloy coatings with different types of TiC reinforcement, Surf. Coat. Technol. 471 (2023) 129910, https://doi.org/10.1016/j.surfcoat.2023.129910.

[23] H. Wu, L. Wang, S. Zhang, C.L. Wu, C.H. Zhang, X.Y. Sun, J. Chen, Tribological properties and sulfuric acid corrosion resistance of laser clad CoCrFeNi high entropy alloy coatings with different types of TiC reinforcement, Tribol. Int. 188 (2023) 108870, https://doi.org/10.1016/j.triboint.2023.108870.

[24] X. Qi, F. Li, Y. Li, J. Du, C. Li, J. Zhao, B. Yang, Microstructure regulation and reinforcement mechanisms of ultrafine TiC/Fe55 composite coatings via laser melting deposition, Mater. Des. 229 (2023) 111924, https://doi.org/10.1016/j.matdes.2023.111924.

[25] S. Bhatnagar, S. Mullick, A study on the influence of reinforcement particle size in laser cladding of TiC/Inconel 625 metal matrix composite, Opt Laser. Technol. 161 (2023) 109115, https://doi.org/10.1016/j.optlastec.2023.109115.

[26] X. Sun, X. Ren, W. Qiang, Y. Feng, X. Zhao, B. Huang, Microstructure and properties of Inconel 718 matrix composite coatings reinforced with submicron TiC particles prepared by laser cladding, Appl. Surf. Sci. 637 (2023) 157920, https://doi.org/10.1016/j.apsusc.2023.157920.

[27] L. Zheng, Z. Liu, H. Zhao, Q. Guo, M. Zhang, Q. Huang, Synthesis and formation mechanism of ZrC–SiC–TiC ceramic powders with high-sinterability via sol-gel process and carbothermal reduction, Ceram. Int. 50 (2024) 2825–2835, https://doi.org/10.1016/j.ceramint.2023.11.004.

[28] Y.-C. Woo, H.-J. Kang, D.J. Kim, Formation of TiC particle during carbothermal reduction of TiO$_2$, J. Eur. Ceram. Soc. 27 (2007) 719–722, https://doi.org/10.1016/j.jeurceramsoc.2006.04.090.

[29] Y. Chen, Y. Deng, H. Zhang, L. Wang, J. Ma, A novel and simple route to synthesis nanocrystalline titanium carbide via the reaction of titanium dioxide and different carbon source, Mater. Sci. Appl. 2 (2011) 1622–1626, https://doi.org/10.4236/msa.2011.211215.

[30] D.E. Grove, U. Gupta, A.W. Castleman, Effect of carbon concentration on changing the morphology of titanium carbide nanoparticles from cubic to cuboctahedron, ACS Nano 4 (2010) 49–54, https://doi.org/10.1021/nn9010413.

[31] D.W. Lee, S. Alexandrovskii, B.K. Kim, Mg-thermal reduction of TiCl$_4$+C$_x$Cl$_4$ solution for producing ultrafine titanium carbide, Mater. Chem. Phys. 88 (2004) 23–26, https://doi.org/10.1016/j.matchemphys.2004.02.005.

[32] H. Zhang, F. Li, Q. Jia, G. Ye, Preparation of titanium carbide powders by sol–gel and microwave carbothermal reduction methods at low temperature, J. Sol. Gel Sci. Technol. 46 (2008) 217–222, https://doi.org/10.1007/s10971-008-1697-0.

[33] H. Preiss, L.-M. Berger, M. Braun, Formation of black glasses and silicon carbide from binary carbonaceous/silica hydrogels, Carbon N Y 33 (1995) 1739–1746, https://doi.org/10.1016/0008-6223(95)00146-1.

[34] J.S. Benjamin, Dispersion strengthened superalloys by mechanical alloying, Metall. Trans. A 1 (1970) 2943–2951, https://doi.org/10.1007/BF03037835.

[35] M.S. El-Eskandarany, Synthesis of nanocrystalline titanium carbide alloy powders by mechanical solid state reaction, Metall. Mater. Trans. 27 (1996) 2374–2382, https://doi.org/10.1007/BF02651892.

[36] M. Razavi, M.R. Rahimipour, R. Mansoori, Synthesis of TiC–Al$_2$O$_3$ nanocomposite powder from impure Ti chips, Al and carbon black by mechanical alloying, J. Alloys Compd. 450 (2008) 463–467, https://doi.org/10.1016/j.jallcom.2006.11.013.

[37] Z.A. Munir, U. Anselmi-Tamburini, Self-propagating exothermic reactions: the synthesis of high-temperature materials by combustion, Mater. Sci. Rep. 3 (1989) 277–365, https://doi.org/10.1016/0920-2307(89)90001-7.

[38] J.J. Moore, H.J. Feng, Combustion synthesis of advanced materials: Part I. Reaction parameters, Prog. Mater. Sci. 39 (1995) 243–273, https://doi.org/10.1016/0079-6425(94)00011-5.

[39] H.H. Nersisyan, J.H. Lee, C.W. Won, Self-propagating high-temperature synthesis of nano-sized titanium carbide powder, J. Mater. Res. 17 (2002) 2859–2864, https://doi.org/10.1557/JMR.2002.0415.

[40] B. Cochepin, V. Gauthier, D. Vrel, S. Dubois, Crystal growth of TiC grains during SHS reactions, J. Cryst. Growth 304 (2007) 481–486, https://doi.org/10.1016/j.jcrysgro.2007.02.018.

[41] S.K. Mishra, L.C. Pathak, Self-propagating high-temperature synthesis (SHS) of advanced high-temperature ceramics, Key Eng. Mater. 395 (2008) 15–38. https://doi.org/10.4028/www.scientific.net/KEM.395.15.

[42] M. Sherif El-Eskandarany, A. Al-Hazza, Mechanically induced self-propagating reaction and consequent consolidation for the production of fully dense nanocrystalline Ti55C45 bulk material, Mater. Char. 97 (2014) 92–100, https://doi.org/10.1016/j.matchar.2014.09.005.

[43] Z.A. Munir, U. Anselmi-Tamburini, M. Ohyanagi, The effect of electric field and pressure on the synthesis and consolidation of materials: a review of the spark plasma sintering method, J. Mater. Sci. 41 (2006) 763–777, https://doi.org/10.1007/s10853-006-6555-2.

[44] M. Biesuz, S. Grasso, V.M. Sglavo, What's new in ceramics sintering? A short report on the latest trends and future prospects, Curr. Opin. Solid State Mater. Sci. 24 (2020) 100868, https://doi.org/10.1016/j.cossms.2020.100868.

[45] C. Manière, U. Kus, G. Chevallier, A. Weibel, L. Durand, J. Huez, D. Delagnes, C. Estournès, How to overcome the main challenges of SPS technology: reproducibility, multi-samples and elaboration of complex shapes, in: Spark Plasma Sintering, Elsevier, 2019, pp. 77–108, https://doi.org/10.1016/B978-0-12-817744-0.00003-9.

[46] U. Anselmi-Tamburini, J.R. Groza, Critical assessment 28: electrical field/current application – a revolution in materials processing/sintering? Mater. Sci. Technol. 33 (2017) 1855–1862, https://doi.org/10.1080/02670836.2017.1341692.

[47] Z. Trzaska, J.-P. Monchoux, Electromigration experiments by spark plasma sintering in the silver–zinc system, J. Alloys Compd. 635 (2015) 142–149, https://doi.org/10.1016/j.jallcom.2015.02.122.

[48] H. Wang, R. Kou, T. Harrington, K.S. Vecchio, Electromigration effect in Fe-Al diffusion couples with field-assisted sintering, Acta Mater. 186 (2020) 631–643, https://doi.org/10.1016/j.actamat.2020.01.008.

[49] R. Orrù, R. Licheri, A.M. Locci, A. Cincotti, G. Cao, Consolidation/synthesis of materials by electric current activated/assisted sintering, Mater. Sci. Eng. R Rep. 63 (2009) 127–287, https://doi.org/10.1016/j.mser.2008.09.003.

[50] O. Guillon, J. Gonzalez-Julian, B. Dargatz, T. Kessel, G. Schierning, J. Räthel, M. Herrmann, Field-Assisted sintering technology/spark plasma sintering: mechanisms, materials, and technology developments, Adv. Eng. Mater. 16 (2014) 830–849, https://doi.org/10.1002/adem.201300409.

[51] M. Suarez, A. Fernandez, J.L. Menendez, R. Torrecillas, U. H, J. Hennicke, R. Kirchner, T. Kessel, Challenges and opportunities for spark plasma sintering: a key technology for a new generation of materials, in: Sintering Applications, InTech, 2013, https://doi.org/10.5772/53706.

[52] L. Cheng, Z. Xie, G. Liu, Spark plasma sintering of TiC ceramic with tungsten carbide as a sintering additive, J. Eur. Ceram. Soc. 33 (2013) 2971–2977, https://doi.org/10.1016/j.jeurceramsoc.2013.04.017.

[53] H. Endo, M. Ueki, H. Kubo, Hot pressing of SiC-TiC composites, J. Mater. Sci. 25 (1990) 2503–2506, https://doi.org/10.1007/BF00638050.

[54] M. Perrut, P. Caron, M. Thomas, A. Couret, High temperature materials for aerospace applications: Ni-based superalloys and γ-TiAl alloys, C R Phys 19 (2018) 657–671, https://doi.org/10.1016/j.crhy.2018.10.002.

[55] J. Cao, T. Sun, Z. Guo, G. Yang, Y. Liang, J. Lin, Enhancement of room-temperature mechanical properties of TiAl alloy by trace addition of C, Mater. Sci. Eng., A 884 (2023) 145598, https://doi.org/10.1016/j.msea.2023.145598.

[56] Novel route to TiAl structural components for aerospace and gas turbines, Met. Powder Rep. 45 (1990) 527, https://doi.org/10.1016/S0026-0657(10)80188-2.

[57] X. Chen, C. Li, X. Bai, H. Liu, S. Xu, Y. Hu, Microstructure, microhardness, fracture toughness, and abrasive wear of in-situ synthesized TiC/Ti-Al composite coatings by cold spraying combined with heat treatment, Coatings 11 (2021) 1034, https://doi.org/10.3390/coatings11091034.

[58] Z. Sun, L. Yang, S. Wang, Q. Wang, Effect of TiC and TiB$_2$ content on properties of TiAl based alloys, IOP Conf. Ser. Earth Environ. Sci. 714 (2021) 032005, https://doi.org/10.1088/1755-1315/714/3/032005.

[59] V. Avdeeva, A. Bazhina, M. Antipov, A. Stolin, P. Bazhin, Relationship between structure and properties of intermetallic materials based on γ-TiAl hardened in situ with Ti$_3$Al, Metals 13 (2023) 1002, https://doi.org/10.3390/met13061002.

[60] D. Bandyopadhyay, R.C. Sharma, N. Chakraborti, The Ti- Al- C system (titanium - aluminum - carbon), J. Phase Equil. 21 (2000) 195–198, https://doi.org/10.1361/105497100770340273.

[61] M. Alsawat, T. Altalhi, N.F. Alotaibi, Z.I. Zaki, Titanium carbide – titanium boride composites by self propagating high temperature synthesis approach: influence of zirconia additives on the mechanical properties, Results Phys. 13 (2019) 102292, https://doi.org/10.1016/j.rinp.2019.102292.

[62] A.V. Linde, I.A. Studenikin, A.A. Kondakov, V.V. Grachev, Thermally coupled SHS processes in layered (Fe$_2$O$_3$ + 2Al)/(Ti + Al)/(Fe$_2$O$_3$ + 2Al) structures: an experimental study, Combust. Flame 208 (2019) 364–368, https://doi.org/10.1016/j.combustflame.2019.07.010.

[63] L. Lutterotti, Maud: a Rietveld analysis program designed for the internet and experiment integration, Acta Crystallogr. Sect. A Found. Crystallogr 56 (2000) s54.

[64] B.-X. Dong, H.-Y. Yang, F. Qiu, Q. Li, S.-L. Shu, B.-Q. Zhang, Q.-C. Jiang, Design of TiC nanoparticles and their morphology manipulating mechanisms by stoichiometric ratios: experiment and first-principle calculation, Mater. Des. 181 (2019) 107951, https://doi.org/10.1016/j.matdes.2019.107951.

[65] S.J. Schneider, C.L. McDaniel, Effect of environment upon the melting point of Al$_2$O$_3$, J Res Natl Bur Stand A Phys Chem 71A (1967) 317, https://doi.org/10.6028/jres.071A.038.

[66] M.A. Lagos, I. Agote, SPS synthesis and consolidation of TiAl alloys from elemental powders: microstructure evolution, Intermetallics 36 (2013) 51–56, https://doi.org/10.1016/j.intermet.2013.01.006.

[67] S. Sarian, Diffusion of 44Ti in TiCx, J. Appl. Phys. 40 (1969) 3515–3520, https://doi.org/10.1063/1.1658229.

[68] Y. Mishin, Chr Herzig, Diffusion in the Ti–Al system, Acta Mater. 48 (2000) 589–623, https://doi.org/10.1016/S1359-6454(99)00400-0.

[69] Y. Yang, Y. Liang, C. Li, J. Lin, Microstructure and mechanical properties of TiAl matrix composites reinforced by carbides, Metals 12 (2022) 790, https://doi.org/10.3390/met12050790.